Draft version October 23, 2012
Preprint typeset using LaTeX style emulateapj v. 5/2/11

arXiv:1210.5654v1 [astro-ph.SR] 20 Oct 2012

PARTICLE-IN-CELL SIMULATIONS OF PARTICLE ENERGIZATION VIA SHOCK DRIFT ACCELERATION FROM LOW MACH NUMBER QUASI-PERPENDICULAR SHOCKS IN SOLAR FLARES

Jaehong Park[1,2], Chuang Ren[1,2,3], Jared C. Workman[4,1], and Eric G. Blackman[1,2]
[1]Department of Physics & Astronomy, University of Rochester, Rochester NY, 14627
[2]Laboratory for Laser Energetics, University of Rochester, Rochester NY, 14623
[3]Department of Mechanical Engineering, University of Rochester, Rochester NY, 14627 and
[4]Department of Physical & Environmental Sciences, Colorado Mesa University, Grand Junction CO, 81501

Draft version October 23, 2012

ABSTRACT

Low Mach number, high beta fast mode shocks can occur in the magnetic reconnection outflows of solar flares. These shocks, which occur above flare loop tops, may provide the electron energization responsible for some of the observed hard X-rays and contemporaneous radio emission. Here we present new 2D particle-in-cell simulations of low Mach number/high beta quasi-perpendicular shocks. The simulations show that electrons above a certain energy threshold experience shock-drift-acceleration. The transition energy between the thermal and non-thermal spectrum and the spectral index from the simulations are consistent with some of the X-ray spectra from RHESSI in the energy regime, $E \lesssim 40 \sim 100$ keV. Plasma instabilities associated with the shock structure such as the modified-two-stream and the electron whistler/mirror instabilities are examined and compared with the numerical solutions of the kinetic dispersion relations.

Subject headings: PIC simulation, solar flares, low Mach number shocks, shock drift acceleration, modified two-stream, whistler and mirror instabilities

1. INTRODUCTION

Low Mach number (M), high plasma beta (β_p) fast mode shocks can occur in the magnetic reconnection outflows of solar flares. Hard X-ray data from Yohkoh and RHESSI has revealed that electrons are energized above flare loop tops and foot points (e.g., Lin et al. 2003). Solar flares are diverse and the associated reconnection events are likely “acceleration environments” with potentially different mechanisms of particle acceleration operating on different scales. One potential source of particle acceleration, seen from analytic predictions (Blackman & Field 1994) and numerical simulations of reconnection configurations in which an obstacle was present (e.g., Forbes 1998; Workman et al. 2011), involves the presence of low Mach number fast shocks in reconnection outflows. These “termination” shocks may contribute to the high energy acceleration observed over some frequency range, studying the potential ways in which these shocks can accelerate particles is well motivated.

Mann et al. (2006, 2009) and Warmuth et al. (2009) suggested an electron energization via shock drift acceleration (hereafter SDA) in a solar flare termination shock. Guo & Giacalone (2010, 2012) performed hybrid simulations for a solar flare termination shock and test electrons are effectively energized via the interaction with pre-existing large-scale magnetic fluctuations. In recent work (Park et al. 2012), we performed a full particle-in-cell (PIC) simulation for purely perpendicular (i.e. magnetic field perpendicular to shock normal), low M/high β_p shocks, where the upstream magnetic field was directed out of the simulation plane. We found that both electrons and ions are participated in SDA.

Termination shocks may however deviate from purely perpendicularity in solar flares, the extent to which is an open question. In the meantime, it is instructive to relax the constraint that the shocks are exactly perpendicular and consider the case of quasi-perpendicularity. The difference is significant because particles can cross back upstream for quasi-perpendicular shocks.

In this paper, we present the results of full PIC simulations for quasi-perpendicular low M/high β_p shocks. The upstream magnetic field makes angles of $\theta_B = 80^\circ, 82^\circ$, and 83.5° respectively to the shock normal and the shocks satisfy the subluminal condition, $V_{sh}/\cos\theta_B < c$, where V_{sh} is the shock speed in the upstream rest frame and c is the speed of light. In such a subluminal shock, electrons can then be reflected at the shock front due to the magnetic mirror effect and gain energy (e.g., Ball & Melrose 2001; Mann et al. 2006, 2009; Warmuth et al. 2009).

One difficulty in performing PIC simulations for SDA in solar flares is that they require sufficiently high energy electrons above the threshold energy for SDA in the simulation to obtain statistically reliable results. The commonly used Maxwellian distribution has too few above the threshold electrons to be used in a simulation. Herein we use a kappa distribution for both ions and electrons with $\kappa = 10$ for the injected particles. This increases the number of high energy electrons but does not significantly alter the original shock structure, which is determined by the bulk of the thermal particles. Although the kappa distribution is used for computational convenience in this paper, the kappa distribution can also be physically a relevant distribution in the outflow driven electron-ion jet (e.g., Yoon et al 2006; Kašparová & Karlický 2009; Mann et al. 2006, 2009; Warmuth et al. 2009).

The goals of this paper are two-fold: (1) studying the formation and structure of such shocks, including the turbulent dissipation mechanism for collisionless shock sustenance and entropy creation, and (2) studying the particle acceleration mechanism relevant for the soft/hard X-ray flux observations in solar flares. We observe the same modified-two-stream instability in the shock transition region as in the perpendicular shocks (Park et al. 2012) which can provide the turbulent dissipation in the downstream. Furthermore, a temperature anisotropy after the shock transition region is found to drive the electron whistler/mirror instabilities.

As we will see, more abundant SDA-accelerated electrons are found in the present simulations of the quasi-perpendicular case compared to the previously simulations of the perpendicular case (Park et al. 2012). In this context, we also extend the theoretical analysis in Mann et al. (2006, 2009); Warmuth et al. (2009) to include the electric potential jump at the shock front (e.g., Ball & Melrose 2001) and generalize the electron energy spectrum. Both our theoretical analysis and our simulations show a transition energy, $E_{\rm trans,p}$, between the thermal and non-thermal photon spectrum that is determined by the minimum angle of θ_B. We find that the transition energy $E_{\rm trans,p}$ and the spectral index δ from theory and our simulation are consistent with some of the X-ray spectra of solar flares from RHESSI (e.g., Altyntsev et al. 2012) in the energy range, $E \lesssim 40 \sim 100$keV. Beyond $E = 40 \sim 100$keV, to maintain the power-law distribution up to $E \sim$MeV, additional mechanisms beyond the shock acceleration studied are required.

The rest of the paper is organized as follows. The simulation setup is described in section 2. The shock structure and particle acceleration are described in section 3. We summarize in section 4.

2. SIMULATION SETUP

We use the fully relativistic PIC code OSIRIS (Fonseca et al. 2002) to study the formation of and particle energization in low-M, high-β_p shocks, where M is the Mach number and β_p is the ratio of thermal to magnetic pressure. To launch a shock, we use the moving wall boundary condition (Langdon et al. 1988; Park et al. 2012) at the right boundary of the 2D simulation box. The moving wall method generates a slowly propagating shock compared to the more standard fixed reflection boundary method, and allows for smaller box sizes and more efficient use of simulation time.

We adopt parameters typical of those found in solar flare reconnection outflows (Tsuneta 1996; Workman et al. 2011) as the upstream conditions for our shock. In particular, we use a plasma density $n = 5\times 10^9/\text{cm}^3$, electron and ion temperatures $T_e = T_i = 0.8\text{keV}(= 9.27\times 10^6\text{K})$, and the upstream magnetic field strength $B = 6$G with $\beta_p \equiv 8\pi n(T_e+T_i)/B^2 = 8.93$. The magnetic field is in the x-y plane and has an angle of $\theta_B = 80°$, $82°$, and $83.5°$ from the shock normal(x-axis) in each simulation. A reduced ion/electron mass ratio of $m_i/m_e = 30$ is used to reduce computational demands. The Alfvén Mach number is chosen to be $M_A \equiv V_1\sqrt{4\pi m_i n}/B = 6.62$, which equates to an upstream plasma flow velocity in the shock rest frame, $V_1 = 0.032c$, for $m_i/m_e = 30$. If the real mass ratio, $m_i/m_e = 1836$, is used for the same M_A, then the upstream flow velocity would be $1226\text{km/s}(= 0.0041c)$. The super-fast-magnetosonic Mach number M satisfies $M \equiv M_A/\sqrt{1+(5/6)\beta_p} = 2.28$. The ratio of the electron cyclotron frequency to the electron plasma frequency is $\Omega_{ce}/\omega_{pe} = 0.0265$. With these upstream values of M_A and β_p, the Rankine-Hugoniot relation (Tidman & Krall 1971) for the shocks with the angles used gives the compression ratio between (2.06,2.50), where the lower and the upper limits are calculated for 2D and 3D, respectively.

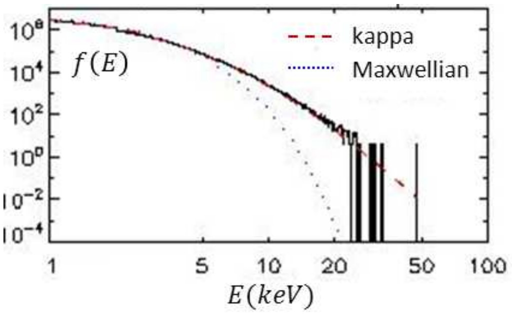

Fig. 1.— The initial energy distribution in the upstream rest frame from the simulation. The dashed line is a kappa distribution with $\kappa = 10$ and $T = 0.8$keV. The dotted line is a Maxwellian distribution with $T = 0.8$keV.

The simulation box is initialized with a kappa–distributed ion-electron plasma drifting with $V_d = 0.0213c$ and $T_e = T_i = 0.8$keV, where V_d is set to a smaller value than the upstream speed $V_1(= 0.032c)$ in the shock rest frame considering the shock to be traveling to the left. In the upstream rest frame, the energy distribution is a kappa distribution such as

$$f(E) = \frac{2^{5/2}}{\sqrt{\pi}}\frac{1}{(2\kappa-3)^{3/2}}\frac{\Gamma(\kappa+1)}{\Gamma(\kappa-1/2)}\frac{E^{1/2}}{T^{3/2}} \times\left(1+\frac{2}{2\kappa-3}\frac{E}{T}\right)^{-\kappa-1}, \qquad (1)$$

where Γ is the gamma function and $f(E)$ is normalized to 1, $\int_0^\infty dEf(E) = 1$. The kappa distribution approaches the Maxwellian distribution as κ goes to ∞. Figure 1 shows the initial energy distribution in the upstream rest frame from the simulation. The dashed line is a kappa distribution in Equation (1) with $\kappa = 10$ and $T = 0.8$keV and the dotted line is a Maxwellian distribution with the same temperature. The bulk parts ($E < 5$ keV) of the two distributions are very similar. The implementation of the kappa distribution in OSIRIS is described in Appendix A.

A uniform external E_z field is set up along the z-axis with $E_z = -V_d B_y/c$. A new plasma of the same kappa distribution is constantly injected from the left boundary ($x = 0$) throughout the simulation. The simulation box sizes are $L_x \times L_y = 250c/\omega_{pe} \times 50c/\omega_{pe}$. The grid size used is $dx = dy = 0.08c/\omega_{pe}$ and the time step used is $dt = 0.056/\omega_{pe}$. For each particle species, 196 particles per cell are used. The particle number/cell is fairly large to reduce numerical collisions and maintain the kappa distribution for a sufficiently long time.

A linear current deposition scheme is used for all simulations in this paper. A periodic boundary condition is used in the y-direction for both particles and fields. For fields, an open boundary condition is used in the x-

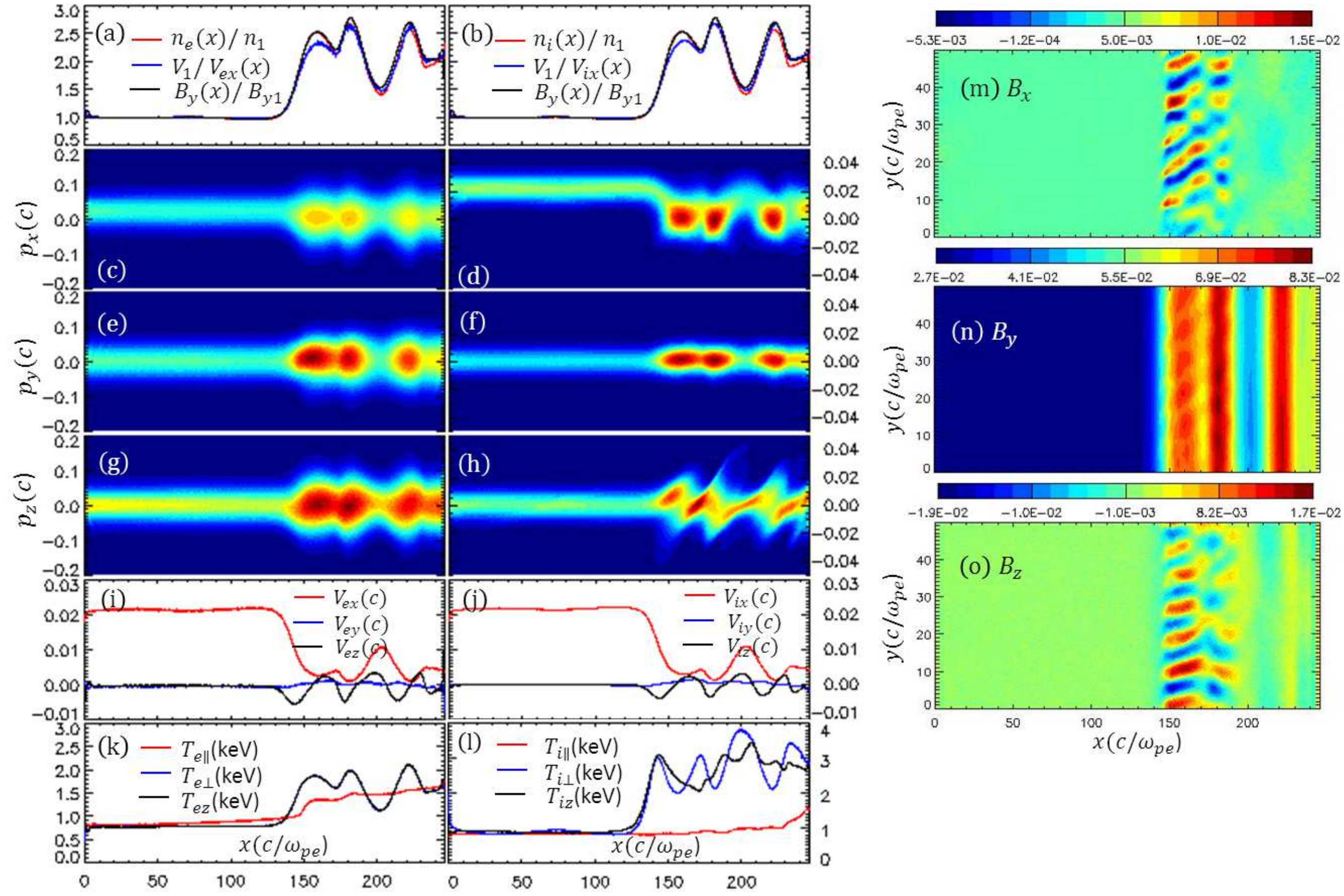

FIG. 2.— The ratios, n/n_1, V_1/V_x, and B_y/B_{y1}, momentum distribution of $p_x - x$, $p_y - x$, and $p_z - x$, y-averaged flow velocity of V_x, V_y, and V_z, and temperature $T_\parallel$, $T_\perp$, T_z for the electrons(left column) and the ions(right column) at $t = 11200/\omega_{pe}$. $(a) \sim (b)$ are calculated in the shock-rest frame and the other plots are obtained in the simulation frame. (m-o) show the B_x, B_y, and B_z fields in the $x - y$ space.

direction. Particles that reach $x = 0$ are re-injected into the box with the initial kappa distribution. At $x = L_x$, a moving wall boundary condition is adopted (Park et al. 2012) and the moving wall speed is set to $V_{\rm wall} = 0.004c$.

3. RESULTS AND ANALYSIS

3.1. *Shock structure*

In Figure 2(a&b), we plot the ratios of downstream to upstream density $n(x)/n_1$, upstream to downstream flow speeds, $V_1/V(x)$, and downstream to upstream y-magnetic field, $B_y(x)/B_{y1}$. In Figure 2(c-l), we plot the phase-space distributions of $p_x - x$, $p_y - x$, and $p_z - x$, the y-averaged flow velocity profiles of $V_x(x)$, $V_y(x)$, and $V_z(x)$, and the temperature profiles of $T_\parallel(x)$, $T_\perp(x)$, and $T_z(x)$ (where $\perp$ and $\parallel$ are perpendicular and parallel to $\mathbf{B}(x)$, respectively), for the electrons (the left column) and the ions (the right column) at $t = 11200/\omega_{pe}$ for the $\theta_B = 80°$ case.

In this subsection, we present results for the shock structure for $\theta_B = 80°$ only but other simulations for $\theta_B = 82°$ and $83.5°$ also show similar shock structures. The electron energization via SDA shows different energy spectra for the different angles of θ_B as we will see in the next subsection.

In Figure 2, the shock front is at $x \approx 140c/\omega_{pe}$ and moves to the left with a speed of $0.01c$ in the simulation frame. In Figure 2(a&b), the compression ratio is $r = 2.5$ near the shock front and oscillates around 2.0 downstream, in reasonable agreement with the Rankine-Hugoniot relation (Tidman & Krall 1971). In Figure 2(c-h), we show that the electrons and ions are heated downstream, but the ions are conspicuously less heated in the y-direction [Figure 2f]. In Figure 2(i&j), the flow velocity, $V_x = 0.021c$, in the upstream decreases downstream to the moving wall speed, $V_{\rm wall} = 0.004c$. The z-component of the velocity, V_z, is oscillating around zero downstream due to the $\mathbf{E}_x \times \mathbf{B}_y$-drift while $V_y \simeq 0$. In Figure 2(k&l), we see that the downstream temperature is anisotropic, that is $T_\perp > T_\parallel$ with $T_{e\perp} = T_{ez} \approx 1.66$keV and $T_{e\parallel} \approx 1.5$keV for the electrons, and $T_{i\perp} = T_{iz} \approx 2.5$keV and $T_{i\parallel} \approx 1.0$keV for the ions.

Figure 2(m-o) show $\mathbf{B}$ in $x - y$ space. The B_x and B_z fields show oscillatory patterns along the y-axis near the shock front ($x \sim 150c/\omega_{pe}$) and the B_y field shows a rippled surface along the y-axis. These variations are due to electron whistler/mirror instabilities driven by the electron temperature anisotropy, $T_{e\perp} > T_{e\parallel}$.

Figure 3 shows the y-averaged $\mathbf{E}$, $\mathbf{B}$, and the potential energy $|e|\Phi(x)(= e\int_{x_1}^{x} E_x dx)$ at $t = 11200/\omega_{pe}$, measured in the shock rest frame. The E_y, E_z, and B_x fields

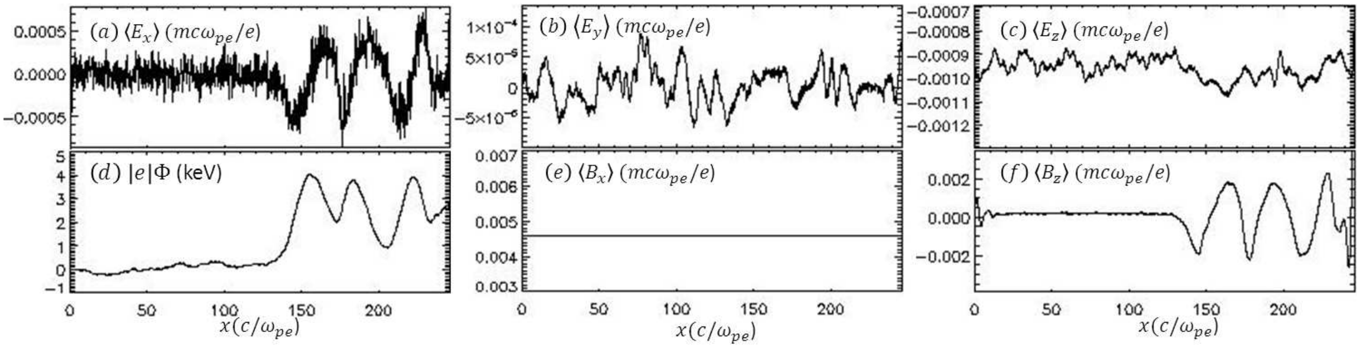

FIG. 3.— y-averaged **E** and **B** fields, and the potential energy $|e|\phi(x)$ at $t = 11200/\omega_{pe}$ measured in the shock rest frame.

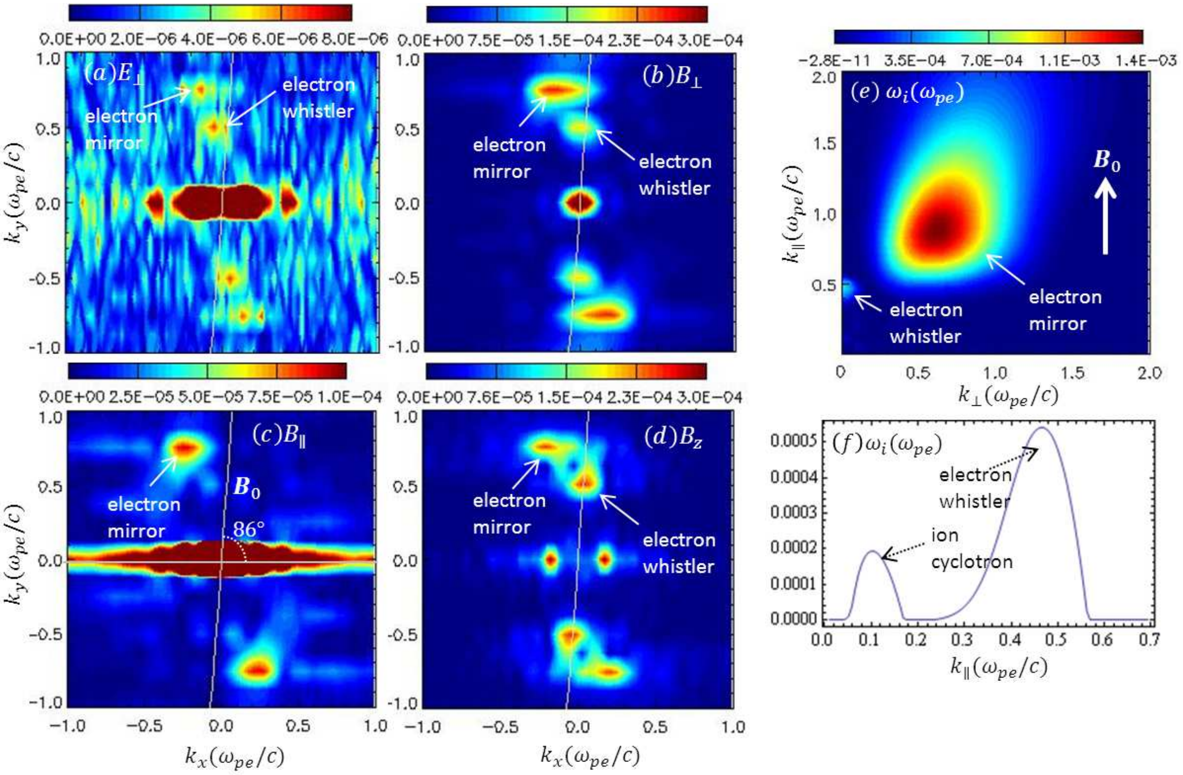

FIG. 4.— (a)∼(d): Fourier spectra of the **E** and **B** fields in the $k_x - k_y$ space from the simulation. The $\mathbf{B}_0$ field has an angle of 86° from the x-axis. (e&f): The growth rates for the electron whistler/mirror modes from the kinetic dispersion relation (Appendix C), (f): The growth rates for the electron whistler/ion cyclotron modes for $\mathbf{k} \times \mathbf{B}_0 = 0$.

are approximately constant across the shock while E_x and B_z oscillate with a wave number $k = 0.2\omega_{pe}/c$ downstream. The potential energy jump $|e|\Delta\Phi$ at the shock front is ~ 3.5keV [Figure 3d]. Some ions in the low energy tail reflect at the shock front and drive the modified two-stream instability.

In Figure 4(a-d), we plot the Fourier spectra of the $E_\perp$, $B_\perp$, $B_\parallel$, and B_z fields, where $\perp$ and $\parallel$ are perpendicular and parallel to $\mathbf{B}_0$, respectively. The $\mathbf{B}_0(= B_{0x}\hat{x} + B_{0y}\hat{y})$ is an averaged field over $150 < x < 170(c/\omega_{pe})$ in Figure 2 and has an angle 86° from the x-axis. The electron whistler and mirror modes driven by electron temperature anisotropy, $T_{e\perp} > T_{e\parallel}$ (e.g., Gary 1993; Gary & Karimabadi 2006) are indicated. The dominant electron whistler mode is along the $\mathbf{B}_0$ with $k = 0.5\omega_{pe}/c$. The dominant mirror mode has $k = 0.8\omega_{pe}/c$ and makes an angle $\theta = 21°$ from $\mathbf{B}_0$. The electron whistler modes are circularly polarized and therefore not seen in the $B_\parallel$ plot [Figure 4c].

To compare the simulation results with the kinetic dispersion relations, we numerically solve the dispersion relation (Appendix C) in Figure 4(e&f). Here we assume that the electron and ion distributions are bi-Maxwellian for simplicity. We use the parameters extracted in the region of $150 < x < 170(c/\omega_{pe})$ at $t = 11200/\omega_{pe}$ in Figure 2(k&l) with $T_{e\parallel} = 1.33$keV and $T_{e\perp} = 1.8$keV for the electrons, and $T_{i\parallel} = 0.85$keV and $T_{i\perp} = 2.3$keV for the ions. The magnetic field strength $B_0 = 16G$. The maximum growth rate for the electron whistler mode is $\omega_i = 5.2 \times 10^{-4}\omega_{pe}$ at $k_\parallel = 0.47(\omega_{pe}/c)$ [Figure 4e&f]. The maximum growth rate for the mirror mode is $\omega_i = 1.4 \times 10^{-3}\omega_{pe}$ at $k_\perp = 0.63$ and $k_\parallel = 0.88(\omega_{pe}/c)$.

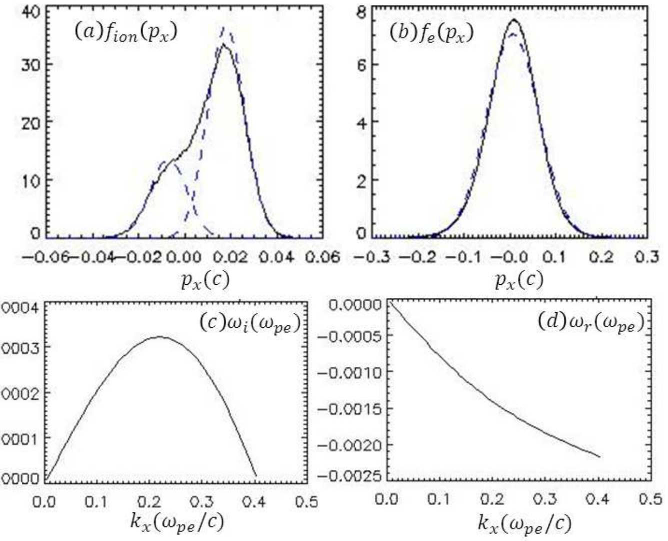

FIG. 5.— (a&b): Ion and electron distributions in the shock transition region, $155 < x < 175(c/\omega_{pe})$ at $t = 8400/\omega_{pe}$. We fit the distributions with Maxwellian distributions(dashed lines). (c&d): The growth rates and real frequencies obtained from the MTSI dispersion relation (Appendix B).

The solutions for the dispersion relation when $\mathbf{k} \times \mathbf{B} = 0$ (Appendix C) and the ion-cyclotron instability weaker than the electron whistler instability are explicitly shown in Figure 4(f).

Figure 5(a&b) shows the electron and ion distributions in the shock transition region in $155 < x < 175(c/\omega_{pe})$ at $t = 8400/\omega_{pe}$. We observe that 27% of the incoming ions are reflected at the shock front [Figure 5a] and the modified two-stream instability (MTSI) can be excited. The MTSI is electrostatic with its wave vector along the x-axis(Appendix B). The electrons have a temperature of $T_{ex} = 1.65$keV and drift with $V_{ex} = 0.0064c$ in the simulation frame [Figure 5b]. We fit the distributions using drifting Maxwellians. The electrons are magnetized with $B = 10G$ while the ions are assumed to be non-magnetized. In the electron rest frame, the drift velocities for the incoming and reflecting ions are $V_{x\mathrm{in}} = 0.0116c$ and $V_{x\mathrm{re}} = -0.0134c$, respectively. Both incoming and reflecting ions have a temperature of $T_{x\mathrm{in}} = T_{x\mathrm{re}} = 0.98$keV. In Figure 5(c&d), we solve the kinetic dispersion relation for the MTSI. The maximum growth rate is $\omega_i = 3.2 \times 10^{-4}\omega_{pe}$ at $k = 0.2c/\omega_{pe}$ and the real frequency is $\omega_r = -0.0015\omega_{pe}$.

Turbulent dissipation is needed to randomize the upstream flow to form collisionless shocks (e.g., Wu 1982). The macroscopic jump conditions across a shock are essentially independent of the source of microphysical turbulence, as long as there is such a source. Plasma instabilities in the shock transition region are natural sources for this needed turbulent dissipation and we consider three possible instabilities: (1)lower hybrid instability (the excited modes are in the $\mathbf{B} \times \nabla\mathbf{B}$ direction) (e.g., Zhou et al. 1983), (2)whistler/mirror instability, and (3)MTSI (e.g., Papadopoulos et al. 1971; Wagner et al. 1971). The lower hybrid instability is precluded in these 2D simulations where the $\mathbf{B}$-field is in the $x - y$ simulation plane. In addition, we notice that the shock structure (i.e. the compression ratio) in the simulation with an in-plane B field is the same as that with the out-of-plane B field which then precludes the whistler/mirror instability. We are led to conclude that the MTSI is the most likely candidate to provide the needed turbulence (e.g., Park et al. 2012).

3.2. *particle heating via shock drift acceleration*

In Figure 6, we plot the electron and ion energy distributions, $f(E)(= dN/dE)$ upstream$(50 < x < 155c/\omega_{pe})$ and downstream$(155 < x < 250c/\omega_{pe})$ at $t = 8400/\omega_{pe}$ for $\theta_B = 80°$. We fit the thermal (bulk) part of the distributions using a kappa distribution with $\kappa = 10$ (dashed lines), yielding $T_e = T_i = 0.8$keV upstream and $T_e = 1.58$keV and $T_i = 1.8$keV downstream. In Figure 6(a&d), we plot the electron and ion phase-space distributions in $E - x$, overlaid with B_y field to indicate the location of the shock front. Abundant non-thermal electrons are seen ahead of the shock at $x = 155c/\omega_{pe}$, traveling as far back as $x = 10c/\omega_{pe}$ [Figure 6a].

In Figure 6(b), the electron energy spectrum shows a deviation from a thermal distribution at $E \sim 12$keV and the spectrum becomes steeper at $E \sim 50$keV. The dotted line in Figure 6(b) is the theoretical energy distribution via SDA when the electric potential energy jump $|e|\Delta\Phi \approx 3.5$(keV) at the shock front is considered (See section 3.2.1). In Figure 6(e), the ion energy spectrum shows a deviation from a thermal distribution at $E \sim 15$keV and the spectrum becomes steeper at $E \sim 30$keV.

In Figure 7(a-d), we plot a typical track of an electron experiencing SDA, overlaid with the shock front and the subsequent compression peaks [Figure 7a]. The electron is reflected at the shock front [Figure 7a] and gains energy from 8keV to 50keV [Figure 7c]. After the reflection, the electron drifts along the upstream magnetic field lines [Figure 7b]. In Figure 7(d), we plot the electron in the $v_\perp - v_\parallel$ phase-space. The electrons in the region I are transferred to the region II after the reflection.

In Figure 7(e&f), we plot a typical track for an ion experiencing SDA. Whether or not an ion gains energy via SDA depends on its incident speed and angle of incidence at the shock front (Kirk 1994). When the ion meets the shock front, it turns back toward the upstream with a larger gyro-radius [Figure 7a] and is accelerated by the E_z field. The kinetic energy of the ion increases from 5keV up to 20keV [Figure 7b]. A detailed analysis for ions experiencing SDA in perpendicular shocks was described in our previous work (Park et al. 2012).

3.2.1. *Electron spectrum via SDA*

In this subsection, we generalize the electron energy spectrum via SDA by Mann et al. (2006, 2009); Warmuth et al. (2009) to include the electric potential jump, $e\Delta\Phi$, at the shock front (e.g., Ball & Melrose 2001) and compare with the PIC simulation results.

First, we consider the de Hoffmann-Teller(dHT) frame (denoted by $'$) where the motional $E_z(= -V_1/cB_y)$ field vanishes. The dHT frame is obtained by boosting with $v_s = V_{sh}/\cos\theta_B$ along the magnetic field line in the upstream rest frame. (Here we consider the negative shock speed, $V_{sh} < 0$, for a shock traveling to the -$\hat{x}$ direction.) The maximum θ_B for the existence of the dHT frame is given by $\theta_{B\max} = \cos^{-1}(V_{sh}/c)(< 90°)$.

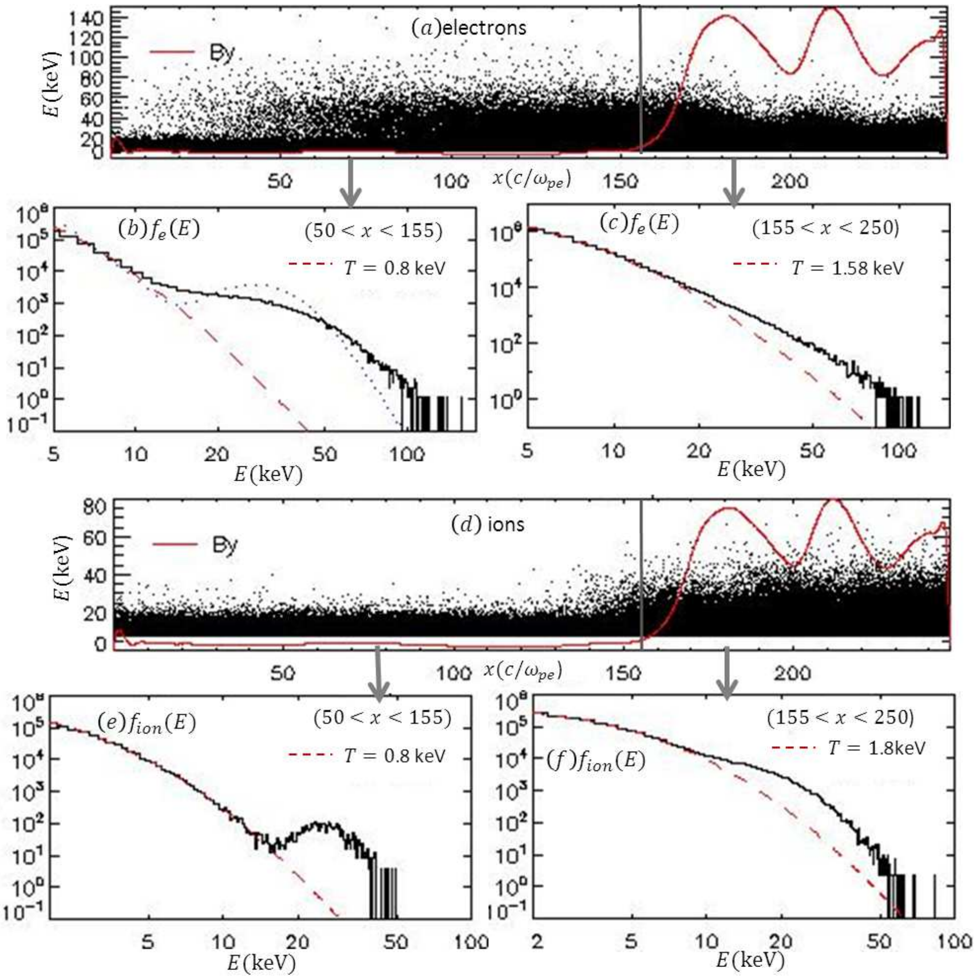

FIG. 6.— (a&d): Energy distribution vs. x-ranges with the B_y field is over-plotted with an arbitrary scale. The electron(b&c) and ion(e&f) energy distributions upstream ($50 < x < 155c/\omega_{pe}$) and downstream ($155 < x < 250c/\omega_{pe}$) at $t = 8400/\omega_{pe}$. In (b), the dotted line is a theoretical energy distribution when the potential energy at the shock front is $e\Phi = -3.5$(keV). We fit the thermal distributions with kappa distributions with $\kappa = 10$(dashed lines).

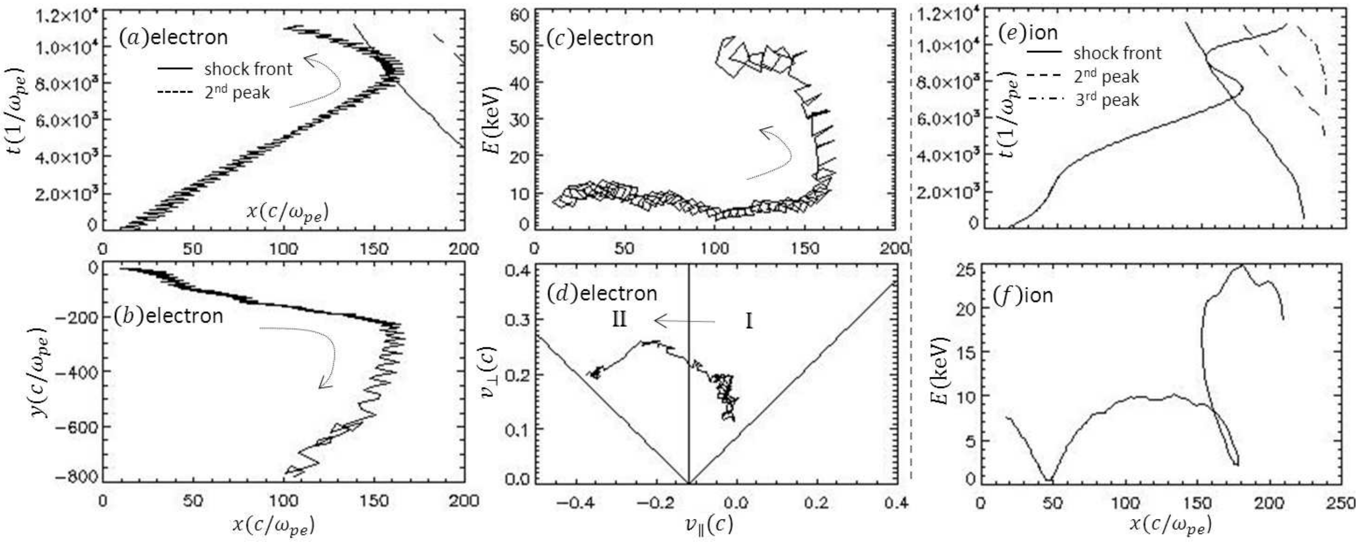

FIG. 7.— (a-d): A typical electron tracking experiencing SDA. (e&f): A typical ion tracking experiencing SDA.

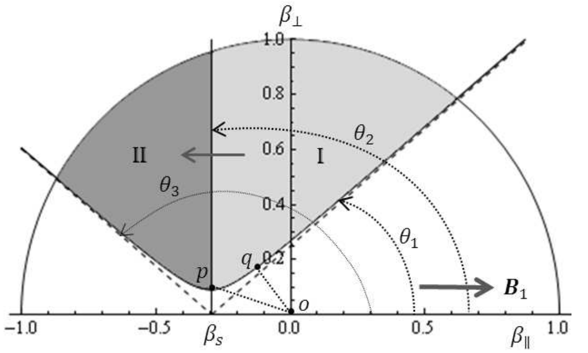

FIG. 8.— The condition for SDA in the $\beta_\parallel - \beta_\perp$ space when $\beta_s = -0.293$. The incoming electrons in the region I(light shaded) are transferred to the region II(dark shaded) after reflection(Mann et al. 2006, 2009). The hyperbolic curve is given by the potential energy $e\Phi = -3.5$keV at the shock front, which approaches the straight dotted lines when $e\Phi \to 0$.

In the dHT frame, the condition for an electron to reflect at the shock front is (e.g., Ball & Melrose 2001; Mann et al. 2006, 2009)

$$\beta'_\perp > \beta'_\parallel \tan\alpha_0 \text{ and } \beta'_\parallel > 0, \tag{2}$$

where $\perp$ and $\parallel$ are perpendicular and parallel to the upstream $\mathbf{B}_1$, respectively, $\beta'_{\parallel,\perp} = v'_{\parallel,\perp}/c$, and $\alpha_0 = \sin^{-1}\sqrt{B_1/B_2}(\approx \sin^{-1}\sqrt{1/r})$. If we include the potential energy $e\Phi(< 0)$ at the shock front, the reflection condition, Equation (2), can be written in the non-relativistic limit by (e.g., Ball & Melrose 2001)

$$\beta'_\perp > \sqrt{\left(\beta'^2_\parallel - \frac{2e\Phi}{m_e c^2}\right)}\tan\alpha_0, \;\; \beta'_\parallel > 0. \tag{3}$$

For relativistic electrons with $\beta'_\parallel \gg \sqrt{2|e|\Phi/m_e c^2}(= 0.117)$, the potential energy $e\Phi$ is negligible and Equation (3) is reduced to Equation (2).

Using the Lorentz transformation between the dHT frame($'$) and the upstream rest frame,

$$\beta'_\parallel = \frac{\beta_\parallel - \beta_s}{1 - \beta_\parallel \beta_s}, \;\; \beta'_\perp = \frac{\beta_\perp}{\gamma_s(1 - v_\parallel \beta_s)}, \tag{4}$$

where $\beta_s = v_s/c(= V_{\rm sh}/(c\cos\theta_B))$ and $\gamma_s = 1/\sqrt{1-\beta_s^2}$, Equation (3) is transformed in the upstream rest frame into

$$\beta_\perp > \gamma_s \tan\alpha_0 \left[(\beta_\parallel - \beta_s)^2 - \frac{2e\Phi}{m_e c^2}(1 - \beta_s\beta_\parallel)^2\right]^{1/2},$$
$$\beta_\parallel > \beta_s. \tag{5}$$

The velocity of the electron after reflection in the dHT frame is given by $\beta'_{r\parallel} = -\beta'_{i\parallel}$ and $\beta'_{r\perp} = \beta'_{i\perp}$, where the indices i and r represent the incoming and reflecting electron, respectively. In the upstream rest frame, one gets (Mann et al. 2006, 2009)

$$\beta_{i\parallel} = \frac{2\beta_s - \beta_{r\parallel}(1+\beta_s^2)}{1 - 2\beta_{r\parallel}\beta_s + \beta_s^2}, \beta_{i\perp} = \frac{\beta_{r\perp}}{\gamma_s^2\left(1 - 2\beta_{r\parallel}\beta_s + \beta_s^2\right)}. \tag{6}$$

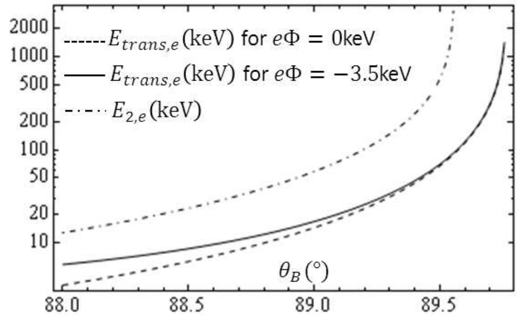

FIG. 9.— The transition energy $E_{\rm trans,e}$ vs θ_B for $e\Phi = -3.5$ keV(solid) and 0 keV(dashed) from Eq.(8). The energy point $E_{2,e}$ vs θ_B(dot-dashed) from Eq.(9). Here $V_{sh} = 0.0041c$, $r = 2.5$ and $m_i/m_e = 1836$ ($M_A = 6.62$ and $\beta_p = 8.93$.)

In Figure 8, we plot the SDA condition in the $\beta_\parallel - \beta_\perp$ space for $\beta_s = -0.293$ as an example (e.g., Mann et al. 2006, 2009). Equation (5) defines the region I(light shaded region) and the hyperbolic curve is given by the potential energy $e\Phi = -3.5$keV at the shock front. When $e\Phi$ goes to zero, the hyperbolic curve approaches the straight lines as seen in Mann et al. (2006, 2009). Equation (6) implies that the incoming electrons in the region I are transferred to the region II (dark shaded region) after reflection. As θ_B increases to $\theta_{B\max}(= \cos^{-1}(V_{sh}/c))$, β_s goes to -1 in Figure 8 and the number of electrons satisfying the reflection condition in Equation (5) decrease to zero. Therefore, no electron reflects at the shock front in the superluminal shocks(where $|\beta_s| \geq 1$) or perpendicular shocks.

The threshold energy $E_{\rm thres}$ for SDA is given by the shortest distance from the origin to the hyperbolic curve, $\overline{oq}(= \beta_{\rm thres})$ in Figure 8, namely

$$E_{\rm thres} = \left(1/\sqrt{1-\beta^2_{\rm thres}} - 1\right) m_e c^2, \text{ where} \tag{7}$$
$$\beta_{\rm thres} = \sqrt{\frac{D^2\left[(1-\beta_s)^2 D^2 P^2 \{P - (1+\beta_s^2)\} + \beta_s^2 - P\right]}{1 + D^2(1 - P\beta_s^2)}},$$

where $D = \gamma_s \tan\alpha_0$ and $P = 2e\Phi/m_e c^2$.

The transition energy $E_{{\rm trans},e}$ between thermal and non-thermal electron populations is given by the distance from the origin to the point p, $\overline{op}(= \beta_{\rm trans})$, in Figure 8 such as

$$E_{{\rm trans},e} = \left(1/\sqrt{1-\beta^2_{\rm trans}} - 1\right) m_e c^2, \text{ where} \tag{8}$$
$$\beta_{\rm trans} = \beta_s^2 - (1-\beta_s^2)(2e\Phi/m_e c^2)\tan^2\alpha_0.$$

The energy point $E_{2,e}$ where the maximum energy ratio of the reflecting to the incoming electron occurs is given by Ball & Melrose (2001) in the non-relativistic approximation, namely

$$E_{2,e} \approx \left(1/\sqrt{1-\beta_2^2} - 1\right) m_e c^2,$$
$$\beta_2 = 2\beta_s \cos(\alpha_0/2), \tag{9}$$

Beyond $E = E_{2,e}$, the spectral index δ, defined as in $f(E) \propto E^{-\delta}$, becomes increasing. Figure 9 shows how the transition energy $E_{{\rm trans},e}$ for $e\Phi = -3.5$ keV(solid)

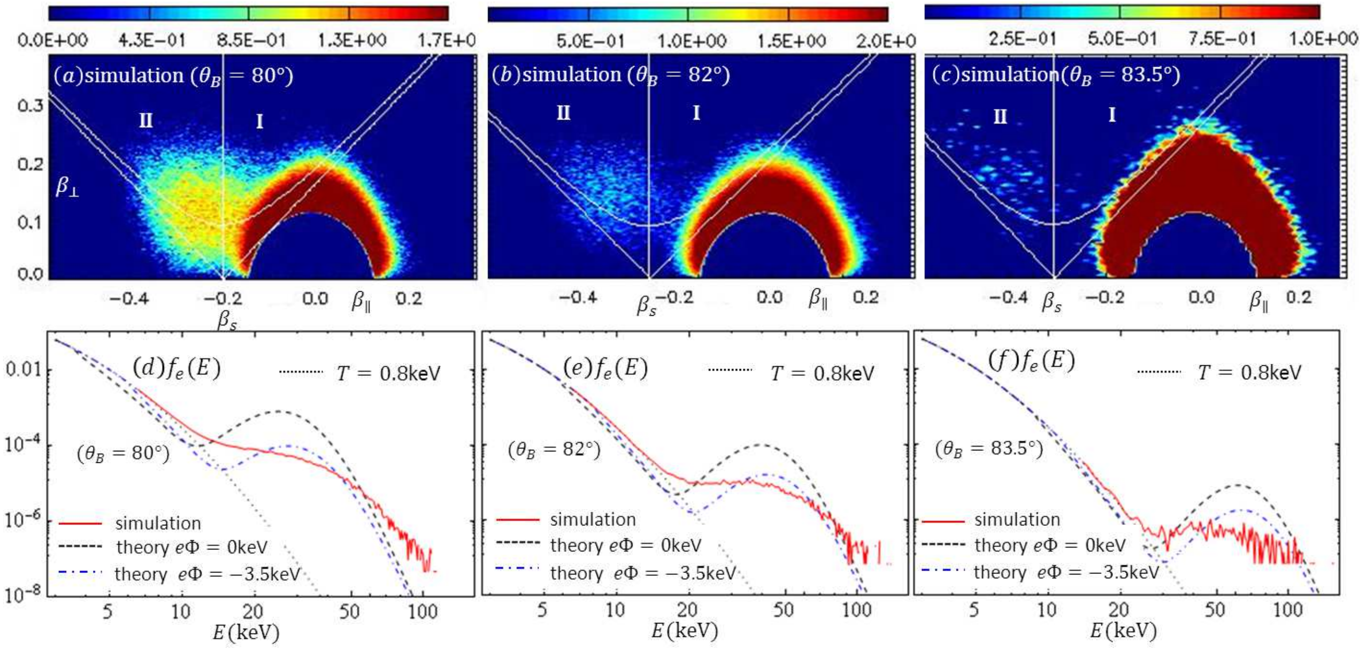

FIG. 10.— (a-c): The upstream electron distribution in the $\beta_\parallel - \beta_\perp$ plane from the simulations for $\theta_B = 80°, 82°$, and $83.5°$. (d∼f): The upstream electron energy distributions in the upstream rest frame from the theoretical distributions with $e\Phi = 0$(dashed) and $e\Phi = -3.5$keV(dot-dashed), and the simulations(solid). We fit the thermal distribution with a kappa distribution with $T = 0.8$keV and $\kappa = 10$(dotted). Here $V_{sh} = -0.032c$, $r = 2.5$ and $m_i/m_e = 30$ ($M_A = 6.62$ and $\beta_p = 8.93$).

and 0 keV(dashed), and $E_{2,e}$(dot-dashed) varies with θ_B when $V_{sh} = 0.0041c$, $r = 2.5$ and $m_i/m_e = 1836$ ($M_A = 6.62$ and $\beta_p = 8.93$).

The reflected electron distribution in the upstream rest frame is written as

$$f_r(\boldsymbol{\beta}_r) = f_i[\boldsymbol{\beta}_i(\boldsymbol{\beta}_r)](d^3\beta_i/d^3\beta_r)\Theta(\beta_s - \beta_{r\parallel})\times \Theta\left(\beta_{r\perp} - \gamma_s \tan\alpha_0 \left[(\beta_s - \beta_{r\parallel})^2 - \frac{2e\Phi}{m_ec^2}(1-\beta_s\beta_{r\parallel})^2\right]^{1/2}\right), \quad (10)$$

where Θ is the step function and the term $d^3\beta_i/d^3\beta_r$ is given by the Jacobian determinant,

$$\frac{d^3\beta_i}{d^3\beta_r} = \frac{\beta_{i\perp}}{\beta_{r\perp}}\left|\frac{\partial(\beta_{i\perp},\beta_{i\parallel})}{\partial(\beta_{r\perp},\beta_{r\parallel})}\right| = \frac{(1-\beta_s)^4}{(1-2\beta_{r\parallel}\beta_s+\beta_s^2)^4}. \quad (11)$$

Here we let the incoming distribution in Equation (10) be a semi-relativistic kappa distribution (Mann et al. 2006, 2009),

$$f_i(\boldsymbol{\beta}_i) = c_\kappa\left(1 + \frac{2(\gamma_i - 1)}{2\kappa - 3}\frac{m_ec^2}{T}\right)^{-\kappa-1}, \quad (12)$$

where $\gamma_i = 1/\sqrt{1-\boldsymbol{\beta}_i^2}$ and $c_\kappa = 1/\int d^3\beta_i f_i(\boldsymbol{\beta}_i)$.

We calculate the upstream electron energy distributions, $f(E) = f(\beta)d\beta/dE$, in the upstream rest frame using Equations (6-12) to obtain

$$f(\beta) = \begin{cases} 2\pi\beta^2\int_{-1}^{1}dt f_i(\beta) \\ \text{.................. for } \beta < \beta_{\rm thres} \\ 2\pi\beta^2\left(\int_{-1}^{t_3}dt + \int_{t_1}^{1}dt\right)f_i(\beta) \\ \text{.................. for } \beta_{\rm thres} \le \beta < \beta_{\rm trans}, \\ 2\pi\beta^2\int_{t_3}^{t_2}dt\frac{d^3\beta_i}{d^3\beta_r}f_i[\boldsymbol{\beta}_i(\beta,t)] \\ +2\pi\beta^2\left(\int_{-1}^{t_2}dt + \int_{t_1}^{1}dt\right)f_i(\beta) \\ \text{.................. for } \beta \ge \beta_{\rm trans} \end{cases} \quad (13)$$

where $t = \cos\theta$ and θ is the electron's pitch angle-the angle between $\boldsymbol{\beta}$ and $\mathbf{B}_1$. The boundaries $t_1(=\cos\theta_1)$, $t_2(=\cos\theta_2)$, and $t_3(=\cos\theta_3)$ as shown in Figure 8 are given as $t_2 = \beta_s/\beta$, and t_1 and $t_3(< t_1)$ are roots of the equation,

$$t_{1,3}^2\left\{1 + D^2\left(1 - P\beta_s^2\right)\right\} - 2t_{1,3}D^2\frac{\beta_s}{\beta}(1-P) + \frac{D^2}{\beta^2}\left(\beta_s^2 - P\right) - 1 = 0. \quad (14)$$

In Figure 10(a-c), we plot the upstream electron distributions in the $\beta_\parallel - \beta_\perp$ plane from the simulations for $\theta_B = 80, 82$ and $83.5°$. We see that electrons in region I are transferred to region II. As θ_B increases, the number of electrons which participate in SDA decrease since the energy threshold for SDA in Equation (7) increases.

In Figure 10(d∼f), we plot the normalized upstream electron energy distributions, $f(E)(= 1/NdN/dE)$, in the upstream rest frame for $\theta_B = 80, 82$ and $83.5°$. We compare the results of Equation (13) for $e\Phi = 0$(dashed) and -3.5(keV)(dot-dashed) with the simulation results(solid). The dotted line is the incoming

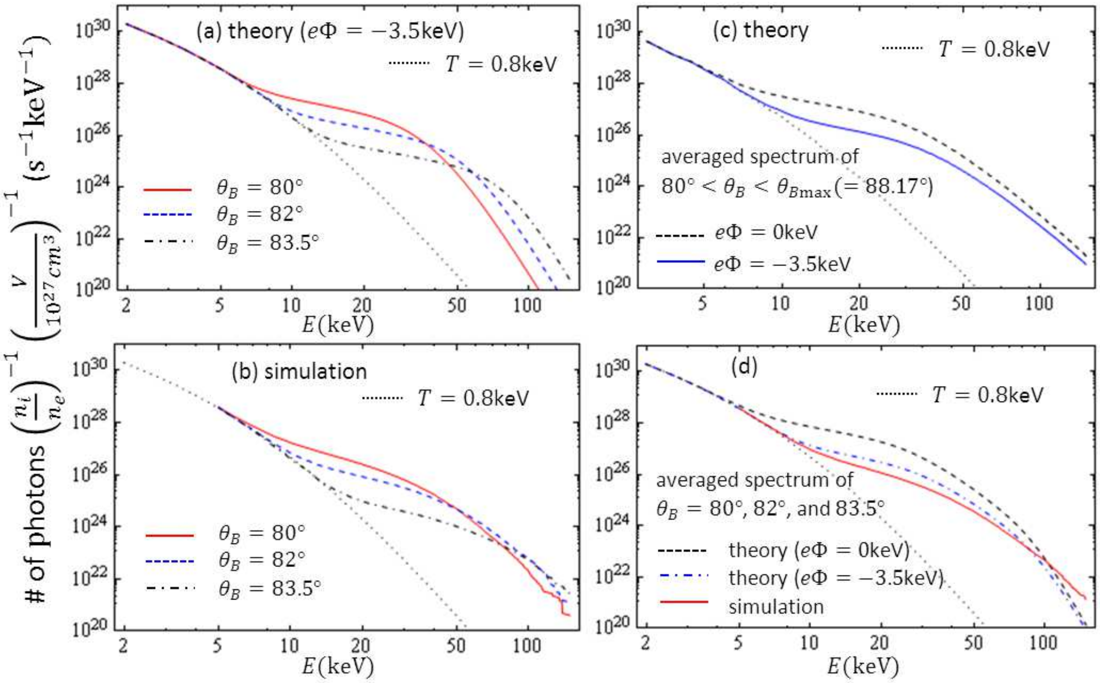

FIG. 11.— (a&b): The photon distribution via bremsstrahlung radiation for $\theta_B = 80°$, $82°$, and $83.5°$ when the electron distributions are given by Eq.(13) and by simulations. (c): The averaged photon distribution of $80° \leq \theta_B \leq \theta_{B\max}(= 88.17°)$ from the theoretical distributions with $e\Phi = 0$ and -3.5keV. (d): The averaged photon distribution of $\theta_B = 80°$, $82°$, and $83.5°$. The dotted line is the photon distribution when the electron distribution is a kappa distribution with $T = 0.8$keV and $\kappa = 10$. Here $V_{sh} = -0.032c$, $r = 2.5$ and $m_i/m_e = 30$ ($M_A = 6.62$ and $\beta_p = 8.93$).

kappa distribution with $T = 0.8$keV and $\kappa = 10$. Using Equation (8), the transition energy points are given by $E_{\text{trans},e} = 11.3$keV, 16.5keV, and 24.2keV for the angles, $\theta_B = 80°$, $82°$, and $83.5°$, respectively, when $e\Phi = -3.5$keV. Using Equation (9), the energy points $E_{2,e}$'s, beyond which the spectral index increases, are given by $E_{2,e} = 34$keV, 56keV, and 93keV for the angles, $\theta_B = 80°$, $82°$, and $83.5°$, respectively. Here $V_{sh} = -0.032c$, $r = 2.5$ and $m_i/m_e = 30$ ($M_A = 6.62$ and $\beta_p = 8.93$).

3.2.2. *Bremsstrahlung radiation*

Electrons accelerated via SDA move along the magnetic field lines as can be seen from the electron tracking in Figure 7(b) and will collide with ions to emit bremsstrahlung radiation. In the low-frequency limit of $\omega b/\gamma v \ll 1$, where ω is a photon angular frequency, b is the impact parameter, v is the electron speed, and $\gamma = 1/\sqrt{1-(v/c)^2}$, the number of photons per unit frequency per unit volume per unit time produced by the bremsstrahlung process is (e.g., Rybicki & Lightman 1979)

$$\frac{dN}{d\omega dV dt} = \frac{16Z^2e^6n_en_i}{3c^3m_e^2\hbar^2\omega}\int_{v_{\min}}^{c}\frac{\gamma}{v}\ln\left(\frac{\gamma m_e v^2}{\hbar\omega}\right)f(v)dv, \tag{15}$$

where $f(v)$ is a normalized electron distribution and $v_{\min}$ is determined by the equation $\hbar\omega = (\gamma_{\min}-1)mc^2$.

Given the electron distributions in Figure 10(d-f), we calculate the number of photons per unit time(sec) per unit energy(keV) using Equation (15) for the ion density of $n_i = n_e$ and the volume of the region emitting the X-rays, $V = 10^{27}\text{cm}^3$. In Figure 11(a&b), we show the photon distribution for $\theta_B = 80$(solid), 82(dashed), and 83.5(dot-dashed) when the electron distribution is given by the theoretical distribution in Equation (13) with $e\Phi = -3.5$keV [Figure 11a] and by the simulation [Figure 11b]. The dotted line is the photon distribution when the electron distribution is given by a kappa distribution with $T = 0.8$keV and $\kappa = 10$. Here $V_{sh} = -0.032c$, $r = 2.5$ and $m_i/m_e = 30$ ($M_A = 6.62$ and $\beta_p = 8.93$).

In Figure 11(c), we plot the averaged photon distribution of $80° \leq \theta_B \leq \theta_{B\max}(= 88.17°)$ from the theoretical distribution in Equation (13) with $e\Phi = 0$(dashed) and $e\Phi = -3.5$keV(solid). In Figure 11(d), we plot the averaged photon distribution of $\theta_B = 80$, 82, and 83.5° from the electron distribution given by Equation (13) with $e\Phi = 0$(dashed) and $e\Phi = -3.5$keV(dot-dashed), and by the simulation(solid). In Figure 11(d), we notice that the theoretical result with $e\Phi = -3.5$keV(dot-dashed) is in good agreement with the simulation result(solid).

In Figure 11(d), the simulation result shows that the transition energy $E_{\text{trans},p}$ between the thermal and non-thermal photon spectrum is $E_{\text{trans},p} \approx 10$keV and the energy point $E_{2,p}$, beyond which the photon spectrum becomes steeper, is $E_{2,p} \approx 40$keV. The spectral index δ is $\delta = 3$(simulation) and $\delta = 2.2$(theory with $e\Phi = -3.5$keV) in 10keV$< E <$ 40keV and $\delta = 7$(simulation) in $E >$ 40keV. For emission from multiple shocks with different θ_B's, the transition energy $E_{\text{trans},p}$ and $E_{2,p}$ would be dominated by the shock with the minimum θ_B. Note that the transition energy $E_{\text{trans},p}$ for the photon distribution is a bit smaller than $E_{\text{trans},e}$ for the elec-

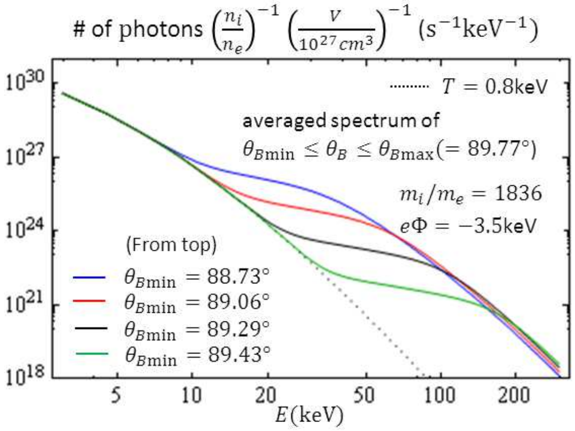

FIG. 12.— The averaged photon distribution of $\theta_{B\min} \le \theta_B \le \theta_{B\max}(= 89.77°)$ from the theoretical distributions in Equation (13) with $e\Phi = -3.5$keV for several minimum values of θ_B. Here $V_{sh} = 0.0041c$, $r = 2.5$ and $m_i/m_e = 1836$ ($M_A = 6.62$ and $\beta_p = 8.93$). The transition energy increases as $\theta_{B\min}$ increases.

tron distribution because bremsstrahlung photons are produced by electrons with higher energies than the photon energy (e.g., Holman 2003). The energy point $E_{2,p}$ is approximately given by Equation (9).

RHESSI data for several solar flares (Table I in Altyntsev et al. (2012)), shows that the spectral index δ is in the range $2.5 < \delta < 3$ and the transition energy is in the range 12.1 keV $< E_{\mathrm{trans},p} <$ 29.2 keV. Therefore, the electron energization via SDA well explains some of the RHESSI X-ray spectra for the energy regime, $E < E_{2,p}$ and how the transition energy is related with the shock geometry, i.e., the minimum θ_B.

The observed RHESSI spectra do not show a steepening beyond $E = E_{2,p}$, and thus the theory herein cannot by itself account for the electron acceleration to produce those photons. This indicates additional mechanisms, such as diffusive shock acceleration, are required for further electron energization to maintain the power-law spectrum up to $E \sim$ MeV. It is not unreasonable to expect that solar flares involve multiple acceleration mechanisms operating on a range of scales.

3.3. *Effects of a realistic proton/electron mass ratio on the spectra*

When the actual ion/electron mass ratio of $m_i/m_e = 1836$ is used, the shock speed in the upstream rest frame is reduced by $\sqrt{30/1836}$ compared to our simulations when the Mach number M and the plasma β_p are fixed. The compression ratio r and the electric potential jump $e\Delta\Phi$ are unchanged for a fixed M and β_p(e.g., Hoshino 2001). Therefore, the shock structure are not expected to change for a realistic mass ratio simulation.

The electron energy spectrum in Equation (6) depends only on β_s, α_0, and $e\Phi$. For a fixed M and β_p, $\alpha_0(\equiv \sin^{-1}\sqrt{B_1/B_2})$ and $e\Phi$ are unchanged. From the definition of $\beta_s(\equiv V_{sh}/c\cos\theta_B)$, we only need to change the angle from θ_B into θ'_B to make the electron energy spectrum unchanged for the mass ratio $m_i/m_e = 1836$ compared to $m_i/m_e = 30$,

$$\theta'_B = \cos^{-1}\left[\frac{\cos\theta_B}{\sqrt{1836/30}}\right]. \tag{16}$$

For example, $80° \le \theta_B \le \theta_{B\max}(= 88.17°)$ for $m_i/m_e = 30$ corresponds to $88.73° \le \theta_B \le 89.77°$ for $m_i/m_e = 1836$.

In Figure 12, we plot the averaged photon distribution of $\theta_{B\min} \le \theta_B \le \theta_{B\max}(= 89.77°)$ for a real ion/electron mass ratio, $m_i/m_e = 1836$, from the electron distribution given by Equation (13) with $e\Phi = -3.5$keV. Here $V_{sh} = 0.0041c$ and $r = 2.5$ ($M_A = 6.62$ and $\beta_p = 8.93$). The different values of $\theta_{B\min}$, from $\theta_{B\min} = 88.73°$ to $89.43°$, give the different transition energy points, from $E_{\mathrm{trans},p}$ = 10 to 35 keV. The power indices of the photon spectrum are nearly the same as $\delta \sim 2.2$ in $E_{\mathrm{trans},p} < E < E_{2,p}$, where $E_{2,p}$ runs from 40 to 150 keV.

4. CONCLUSION

In summary, we studied quasi-perpendicular, low M/high β_p shocks with full PIC 2-D simulations using a reduced ion/electron mass ratio $m_i/m_e = 30$. The shock compression ratio we found was in agreement with the Rankine-Hugoniot relation. Electron whistler/mirror instabilities driven by downstream temperature anisotropy were observed. A modified two-stream instability due to the incoming and reflecting ions in the shock transition region was also observed.

Abundant non-thermal electrons accelerated via SDA were observed upstream. We compared the electron energy distribution from the simulation with the distributions derived by extending a theoretical model (Mann et al. 2006, 2009; Warmuth et al. 2009) to include electric potential energy at the shock front, and found good agreement.

In perpendicular shocks, however, SDA can be achieved only by particles transmitted into the downstream, and the energy obtained by the transmitted particles are smaller than that by the reflected ones (e.g., Ball & Melrose 2001). Therefore, such abundant non-thermal electrons observed in quasi-perpendicular shocks in this paper are not seen in perpendicular shocks (e.g., Park et al. 2012).

We calculated the photon flux via bremsstrahlung radiation from the electron distributions from both the theory and simulation and we identified a transition energy, $E_{\mathrm{trans},p}$ marking the change between a thermal and non-thermal photon spectrum. $E_{\mathrm{trans},p}$ is determined by the minimum θ_B from multiple shocks with different θ_B's in $\theta_{B\min} \le \theta_B \le 90°$. Different solar flares have different $\theta_{B\min}$'s in their termination shocks and therefore show different transition energy points.

From the simulations, the averaged photon spectrum of $\theta_B = 80°$, $82°$, and $83.5°$ gives a spectral index $\delta \sim 3$ in 10keV$< E <$ 40keV and the spectral index increases beyond $E =$ 40keV. The spectral index $\delta \sim 3$ as well as the transition energy, $E_{\mathrm{trans},p} =$ 10keV, well explains some of the RHESSI X-ray spectra in the energy regime, $E <$ 40keV. To account the spectral index of the RHESSI X-ray spectrum up to E ∼MeV, however, additional mechanisms other than SDA are required.

Note that although our simulations were performed using $m_i/m_e = 30$, we analytically scaled the results to the realistic ion/electron mass ratio, and found that the predicted photon spectra are indeed insensitive to this mass ratio.

This work was supported by NSF under Grant PHY-0903797, by DOE under Grant No. DE-FG02-06ER54879 and Cooperate Agreement No. DE-FC52-08NA28302, and by NSFC under Grant No. 11129503. We also thank the OSIRIS consortium for the use of OSIRIS. The research used resources of NERSC.

APPENDIX

GENERATION OF A KAPPA DISTRIBUTION

To generate a kappa distribution, we use the random number distribution by Leitner et al. (2011). We denote $\{N_i(0,1)|i = 1, 2, ..., N\}$ as a set of normally distributed random numbers with the mean of 0 and the deviation of 1, and $\{U_i(0,1)|i = 1, 2, ..., N\}$ as a set of uniformly distributed random numbers between [0,1]. Then a sequence of the random number x_i given by

$$x_i = b_1 N_i(0,1) + b_2 U_i(0,1) x_{i-1} \tag{A1}$$

generates a 1D kappa distribution with the mean of 0 and the deviation of 1, and the coefficients, b_1 and b_2 determine the index κ (Figure 8 in Leitner et al. 2011).

To implement the kappa generator in OSIRIS, we determine the particle's initial momentum $\mathbf{p}$ as

$$\mathbf{p}_i = \mathbf{p}_{th} x_i + \mathbf{p}_d, \tag{A2}$$

where x_i is given by Equation (A1), $\mathbf{p}_{th}$ and $\mathbf{p}_d$ are the thermal and the drift momentum, respectively. For $\kappa = 10$, we choose $b_1 = 0.58$ and $b_2 = 1.15$. Then a sequence of $\mathbf{p}_i$ in Equation (A2) generates a 3D kappa distribution in Figure 1.

DISPERSION RELATION FOR THE MODIFIED TWO-STREAM INSTABILITY

The kinetic dispersion relation for electrostatic instabilities is

$$1 + \sum_{s=e,i} K_s(\mathbf{k}, \omega) = 0, \tag{B1}$$

where $K_s(\mathbf{k}, \omega)$ is the susceptibility. For magnetized electrons with isotropic Maxwellian distributions, $K_e(\mathbf{k}, \omega)$ is given by (Gary 1993)

$$K_e(\mathbf{k}, \omega) = \frac{\omega_{pe}^2}{v_{eth}^2 k^2} \left[1 + \xi_e^0 e^{-\lambda_e} \sum_{m=-\infty}^{\infty} I_m(\lambda_e) Z(\xi_e^m) \right], \tag{B2}$$

where v_{eth} is the thermal velocity, I_m is the modified Bessel function of the first kind, $\lambda_e = k_\perp^2 v_{eth}^2/\Omega_e^2$, $\Omega_e = eB/(m_e c)(< 0)$, Z is the plasma dispersion function, and $\xi_e^m = (\omega - m\Omega_e)/(\sqrt{2} k_\parallel v_{eth})$. For unmagnetized ions with drifting Maxwellian distributions,

$$K_i(\mathbf{k}, \omega) = -\frac{\omega_{pi}^2}{2 v_{ith}^2 k^2} Z'(\xi_i), \tag{B3}$$

where $\xi_i = (\omega - \mathbf{k} \cdot \mathbf{V}_{id})/(\sqrt{2} k v_{ith})$ and $'$ is the derivative with respect to ξ_s.

Here we consider that $\mathbf{B} \approx B_y \hat{y}$, $\mathbf{k} = k_x \hat{x}$ $\mathbf{V}_{sd} = V_{sd} \hat{x}$. Then the term $\xi_e^0 Z(\xi_s^m)$ in Equation (B2) becomes $-\omega/(\omega - m\Omega_e)$ as $k_\parallel$ goes to 0. The dispersion relation for the MTSI becomes

$$1 + \frac{\omega_{pe}^2}{v_{eth}^2 k^2} \left(1 - e^{-\lambda_e} \sum_{m=-\infty}^{\infty} I_m(\lambda_e) \frac{\omega}{\omega - m\Omega_e} \right) - \sum_{s=in,re} \frac{\omega_{ps}^2}{2 v_{sth}^2 k^2} Z'(\xi_s) = 0. \tag{B4}$$

DISPERSION RELATION FOR BI-MAXWELLIAN DISTRIBUTIONS

The kinetic dispersion relation for electromagnetic instabilities is

$$\det \left(k_i k_j - k^2 \delta_{ij} + \frac{\omega^2}{c^2} \delta_{ij} + k^2 \sum_{s=e,i} S_{sij} \right) = 0, \tag{C1}$$

where S_{sij} is the conductivity tensor. Here we consider that $\mathbf{k} = k_x \hat{x} + k_z \hat{z}$, $\mathbf{B}_0 = B_0 \hat{z}$, and the electrons and ions have bi-Maxwellian distributions. Following Gary (1993), we get

$$S_{sxx} = \frac{\omega_s^2}{k^2 c^2} \frac{e^{-\lambda_s}}{\lambda_s} \left[\xi_s^0 \sum_{m=-\infty}^{\infty} m^2 I_m(\lambda_s) Z(\xi_s^m) - \frac{1}{2} \left(\frac{T_{s\perp}}{T_{s\parallel}} - 1 \right) \sum_{m=-\infty}^{\infty} m^2 I_m(\lambda_s) Z'(\xi_s^m) \right], \tag{C2}$$

$$S_{sxy} = -i \frac{\omega_s^2}{k^2 c^2} e^{-\lambda_s} \left[\xi_s^0 \sum_{m=-\infty}^{\infty} m \left\{ I_m(\lambda_s) - I_m'(\lambda_s) \right\} Z(\xi_s^m) - \frac{1}{2} \left(\frac{T_{s\perp}}{T_{s\parallel}} - 1 \right) \sum_{m=-\infty}^{\infty} m \left\{ I_m(\lambda_s) - I_m'(\lambda_s) \right\} Z'(\xi_s^m) \right], \tag{C3}$$

$$S_{sxz} = -\frac{\omega_s^2}{k^2 c^2} \frac{e^{-\lambda_s}}{\lambda_s} \left[\xi_s^0 \frac{k_x v_{sth\parallel}}{\sqrt{2} \Omega_s} \frac{T_{s\perp}}{T_{s\parallel}} \sum_{m=-\infty}^{\infty} m I_m(\lambda_s) Z'(\xi_s^m) - \frac{1}{2} \frac{k_x}{k_z} \left(\frac{T_{s\perp}}{T_{s\parallel}} - 1 \right) \sum_{m=-\infty}^{\infty} m^2 I_m(\lambda_s) Z'(\xi_s^m) \right], \tag{C4}$$

$$S_{syy} = \frac{\omega_s^2}{k^2 c^2} e^{-\lambda_s} \left[\xi_s^0 \sum_{m=-\infty}^{\infty} \left\{ 2\lambda_s (I_m - I_m') + \frac{m^2}{\lambda_s} I_m \right\} Z_m - \frac{1}{2} \left(\frac{T_{s\perp}}{T_{s\parallel}} - 1 \right) \sum_{m=-\infty}^{\infty} \left\{ 2\lambda_s (I_m - I_m') + \frac{m^2}{\lambda_s} I_m \right\} Z_m' \right], \tag{C5}$$

$$S_{syz} = -\frac{i}{2} \frac{\omega_s^2}{k^2 c^2} \frac{k_x}{k_z} e^{-\lambda_s} \left[\frac{\omega}{\Omega_s} \frac{T_{s\perp}}{T_{s\parallel}} \sum_{m=-\infty}^{\infty} (I_m - I_m') Z_m' - \left(\frac{T_{s\perp}}{T_{s\parallel}} - 1 \right) \sum_{m=-\infty}^{\infty} m (I_m - I_m') Z_m' \right], \tag{C6}$$

$$S_{szz} = -\frac{\omega_s^2}{k^2c^2}e^{-\lambda_s}\left[\xi_s^0\sum_{m=-\infty}^{\infty} I_m(\lambda_s)\xi_s^m Z'(\xi_s^m) - \frac{1}{\sqrt{2}}\frac{\Omega_s}{k_z v_{sth\parallel}}\left(1-\frac{T_{s\parallel}}{T_{s\perp}}\right)\sum_{m=-\infty}^{\infty} m I_m(\lambda_s)\xi_s^m Z'(\xi_s^m)\right], \tag{C7}$$

$$S_{syx} = -S_{sxy},\ S_{szx} = S_{sxz},\ S_{szy} = -S_{syz}, \tag{C8}$$

where $\lambda_s = k_\perp^2 v_{sth}^2/\Omega_s^2$ and $\xi_s^m = (\omega - m\Omega_s)/(\sqrt{2}k_\parallel v_{sth})$.

When $\mathbf{k} \times \mathbf{B_0} = 0$, the dispersion relation, Equation (C1), reduces to

$$-k^2 + \frac{\omega^2}{c^2} + k^2\sum_{s=e,i} S_s^{\pm} = 0, \tag{C9}$$

where $S_s^{\pm}$ is given by

$$S_s^{\pm} = \frac{\omega_{ps}^2}{k^2c^2}\left[\xi_s^0 Z(\xi_s^{\pm 1}) - \frac{1}{2}\left(\frac{T_{s\perp}}{T_{s\parallel}} - 1\right)Z'(\xi_s^{\pm 1})\right]. \tag{C10}$$

REFERENCES

Altyntsev, A. A., Fleishman, G. D., Lesovoi, S. V., & Meshalkina, N. S. 2012, ApJ, 758, 138

Ball, L. & Melrose, D. B. 2001, Publ, Astron. Soc Aust., 18, 361

Blackman, E. G. & Field, G. B. 1994, PRL, 73, 3097

Fonseca, R. A., et al. 2002, Lect. Notes Comput. Sci., 2331, 342

Forbes, T.G. 1998, Solar Physics, 117, 97

Gary, S. P. 1993, Theory of Space Plasma Microinstabilities, (Cambridge Univ. Press, Cambridge)

Gary, S. P. & Karimabadi, H. 2006, J. Geophy. Res., 111, A11224

Guo, F. & Giacalone, J. 2010, ApJ, 715, 406

Guo, F. & Giacalone, J. 2012, ApJ, 753, 28

Hoshino, M. 2001, Prog. Theo. Phys. Suppl. 143, 149

Holman, G. D., Sui, L., Schwartz, R. A, & Emslie, G, 2003, ApJ, 595, L97

Kašparová, J. & Karlický, M. 2009, A&A, 497, L13

Kirk, J. G. 1994, in Plasma Astrophysics, ed. Kirk, J. G., Melrose, D. B., & Priest, E. R.(Springer-Verlag, Berlin)

Langdon, B., Arons, J., & Max, C. 1988, PRL, 61, 7

Leitner, M., Leubner, M. P., & Vörös, Z. 2011, Physica A, 390, 124

Lin R. P., Krucker, S., Hurford, G. J., et al. 2003, ApJ, 595, L69

Mann, G., Aurass, H., & Warmuth, A. 2006, A&A, 454, 969

Mann, G., Warmuth, A., & Aurass, H. 2009, A&A, 494, 669

Papadopoulos, K., Wagner, C. E., & Haber, I. 1971, PRL 27, 982

Park, J., Workman, J. C., Blackman, E. G., Ren, C., & Siller, R. 2012, Phys. Plasmas, 19, 062904

Rybicki, G. B. & Lightman, A. P. 1979, Radiative Processes in Astrophysics(John Wiley & Sons, New York)

Tidman, D. A. & Krall, N. A. 1971, Shock Waves in Collisionless Plasmas (Wiley-Interscience, New York)

Tsuneta, S. 1996, ApJ, 456, 840

Wagner, E., Papadopoulos, K., & Haber, I. 1971, Phys. Lett. A 35, 440

Warmuth, A., Mann, G., & Aurass, H. 2009, A&A, 494, 677

Workman, J. C., Blackman, E. G., & Ren, C. 2011, Phys. Plasmas, 18, 092902

Wu, C. S. 1982, Space Science Rev., 32, 83

Yoon, P. H., Rhee, T., & Ryu, J. 2006, Geophy., 111, A09106

Zhou, Y. M., Wong, H. K., Wu, C. S., & Winske, D. 1983, J. Geophys. Res., 88, 3026